



Laboratory and Astronomical Discovery of Magnesium Dicarbide, MgC₂

P. B. Changala¹ , H. Gupta^{1,2} , J. Cernicharo³ , J. R. Pardo³ , M. Agúndez³ , C. Cabezas³ , B. Tercero⁴ ,
M. Guélin⁵ , and M. C. McCarthy¹

¹ Center for Astrophysics | Harvard & Smithsonian, Cambridge, MA 02138, USA; bryan.changala@cfa.harvard.edu

² National Science Foundation, Alexandria, VA 22314, USA

³ Instituto de Física Fundamental, CSIC, Department of Molecular Astrophysics, Serrano 121, E-28006 Madrid, Spain

⁴ Observatorio Astronómico Nacional, IGN, C/Alfonso XII 3, E-28014 Madrid, Spain

⁵ Institut de Radioastronomie Millimétrique, 300 rue de la Piscine, F-38406 Saint Martin d'Hères, France

Received 2022 October 19; accepted 2022 November 7; published 2022 November 29

Abstract

We report the detection of magnesium dicarbide, MgC₂, in the laboratory at centimeter wavelengths and assign ²⁴MgC₂, ²⁵MgC₂, and ²⁶MgC₂ to 14 unidentified lines in the radio spectrum of the circumstellar envelope of the evolved carbon star IRC+10216. The structure of MgC₂ is found to be T-shaped with a highly ionic bond between the metal atom and the C₂ unit, analogous to other dicarbides containing electropositive elements. A two-temperature excitation model of the MgC₂ emission lines observed in IRC+10216 yields a very low rotational temperature of 6 ± 1 K, a kinetic temperature of 22 ± 13 K, and a column density of (1.0 ± 0.3) × 10¹² cm⁻². The abundance of MgC₂ relative to the magnesium–carbon chains MgCCH, MgC₄H, and MgC₆H is 1:2:22:20 and provides a new constraint on the sequential radiative association–dissociative recombination mechanisms implicated in the production of metal-bearing molecules in circumstellar environments.

Unified Astronomy Thesaurus concepts: [Circumstellar envelopes \(237\)](#); [Metal-containing molecules \(2258\)](#); [Laboratory astrophysics \(2004\)](#); [Carbon stars \(199\)](#)

1. Introduction

Silicon dicarbide (SiC₂) was long known to exist in carbon-rich stellar atmospheres (Kleman 1956, and references therein), but its identification as the carrier of nine unassigned lines in the radio spectrum of the archetype carbon star IRC+10216 was a key advance in understanding the molecular constituents of evolved carbon stars (Thaddeus et al. 1984). Its substantial abundance and the highly ionic nature of the Si–C₂ bond suggested that molecules containing other electropositive elements bonded to C₂ or longer carbon chains might be present in IRC+10216 and responsible for other unidentified lines there. In the nearly 40 years since the radio astronomical identification of SiC₂, a number of metal-bearing molecules have been discovered in IRC+10216, most containing strong ionic bonds between metal atoms and carbon chains (Cernicharo et al. 2019; Pardo et al. 2021). It is surprising, therefore, that metal dicarbides—the simplest molecules containing one metal atom and two carbon atoms—are absent from this inventory. Although several metal dicarbides have now been studied in the laboratory, accurate data are available only for one (AlC₂; Halfen & Ziurys 2018, & references therein) that is a plausible candidate for radio astronomical detection.

Magnesium dicarbide (MgC₂) is an excellent candidate for detection in IRC+10216 because of the high cosmic abundance of magnesium, which is found in nearly half of all known metal-bearing species in this source. An early theoretical study of MgC₂ (Green 1984) predicted a triangular, symmetric, and highly polar ground-state structure similar to SiC₂. Motivated by the discoveries of MgNC and MgCN several years later (Kawaguchi et al. 1993; Ziurys et al. 1995), more accurate

calculations of MgC₂ appeared in the literature (Itono et al. 2000), but no gas-phase measurements followed. The purpose of this Letter is to report the laboratory detection of MgC₂ at centimeter wavelengths, and its assignment to a series of previously unidentified lines in the radio spectrum of IRC+10216. Figure 1 summarizes the laboratory and astronomical measurements and the derived structure of MgC₂. To our knowledge, this is the first spectroscopic characterization of MgC₂ in any wavelength region, while its astronomical discovery fills a longstanding gap in the molecular inventory of evolved carbon stars.

2. Laboratory Measurements

Rotational lines of MgC₂ were detected with a Fourier transform microwave (FTMW) spectrometer coupled to a laser ablation supersonic expansion source previously used in our laboratory to characterize small metal-containing molecules (Brünken et al. 2008; Zingsheim et al. 2017; Lee et al. 2019). A rotating magnesium rod was ablated by 50 mJ pulses of 532 nm radiation from an Nd:YAG laser operating at 5 Hz. The ablated Mg atoms were entrained in a dilute mixture (0.1%) of acetylene in neon, which then passed through two copper discharge electrodes. An 800 V discharge struck between the electrodes increased the product yield by up to a factor of 5 (Sun et al. 2010). After expanding into a large vacuum chamber, the molecules were polarized in a coaxially aligned cavity spectrometer operating from 5 to 26 GHz (Grabow et al. 2005; Crabtree et al. 2016). Double-resonance transitions at higher frequencies were driven by microwave horns placed perpendicular to the cavity axis.

The identification of MgC₂ was challenging because only one transition, the 1₀₁ – 0₀₀ line predicted to lie near 20.9 GHz (Itono et al. 2000), falls within our spectrometer bandwidth. After optimizing the production of MgCCH, we conducted a search from 20.4 to 21.0 GHz. This survey was extremely sparse, with



Original content from this work may be used under the terms of the [Creative Commons Attribution 4.0 licence](#). Any further distribution of this work must maintain attribution to the author(s) and the title of the work, journal citation and DOI.

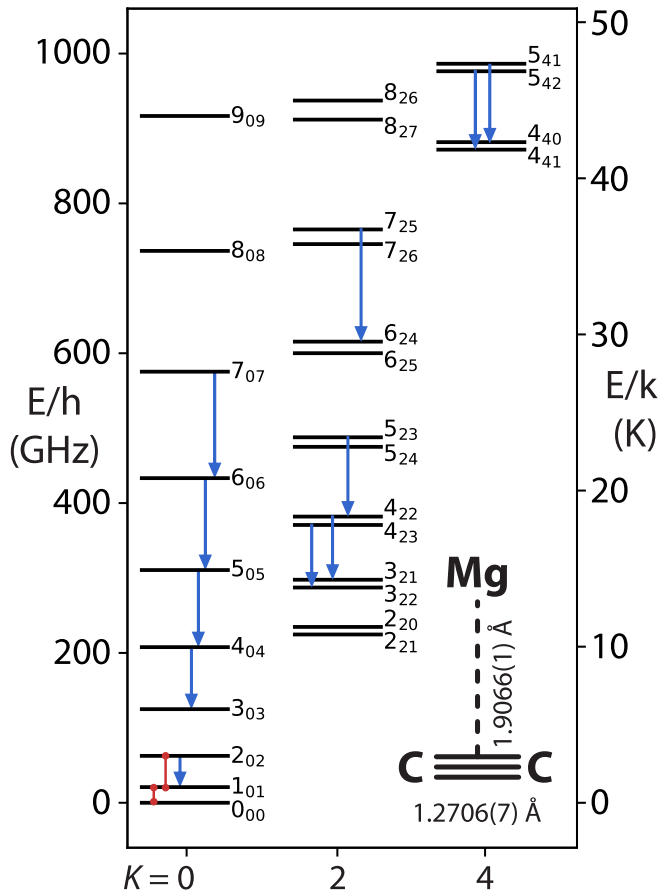


Figure 1. Lower rotational energy levels of MgC_2 . Red lines indicate the observed laboratory transitions and blue arrows the astronomical transitions. The inset shows the semiexperimental equilibrium structure.

only a single ablation-dependent feature at 20896 MHz, shown in Figure 2, close to the prediction of 20892 MHz from quantum chemical calculations performed for this work (see Appendix A). We conducted a number of assays to test the carrier of this line: the signal was unaffected by applied magnetic fields, consistent with the predicted closed-shell ground electronic state; it required the presence of acetylene, but was unaffected by replacing HCCH with DCCD, indicating it contains carbon but not hydrogen; and the relative intensity from a statistical $^{12}\text{C}/^{13}\text{C}$ HCCH precursor suggested it likely contained only two C atoms. Spectroscopic confirmation was provided by the observation of a double-resonance transition ($2_{02} - 1_{01}$, top panel of Figure 2) at its expected frequency near 41.7 GHz. Assuming a dipole moment of 7.9 D (Itono et al. 2000), we estimate the number of MgC_2 molecules in each gas pulse to be 4×10^8 , significantly less abundant than MgCCH (5×10^{10}) or the precursor Mg atoms (5×10^{14} , estimated from the ablation target mass loss) and HCCH (2×10^{15} , from calibrated flow meters).

With the assignment of MgC_2 secure, we proceeded to search for its isotopologues. The fundamental transitions of $^{26}\text{Mg}^{12}\text{C}_2$ and $^{25}\text{Mg}^{12}\text{C}_2$ were detected in natural abundance, while those of $^{24}\text{Mg}^{13}\text{C}^{12}\text{C}$ and $^{24}\text{Mg}^{13}\text{C}_2$ were detected using a ^{13}C -enriched sample of acetylene. Their transition frequencies are shown in Table 1 and are uniformly within 0.5 MHz of the theoretical isotopic shifts. These laboratory measurements are insufficient to determine the A , B , and C rotational constants for each isotopologue independently, but together provide enough information to derive a semiexperimental equilibrium

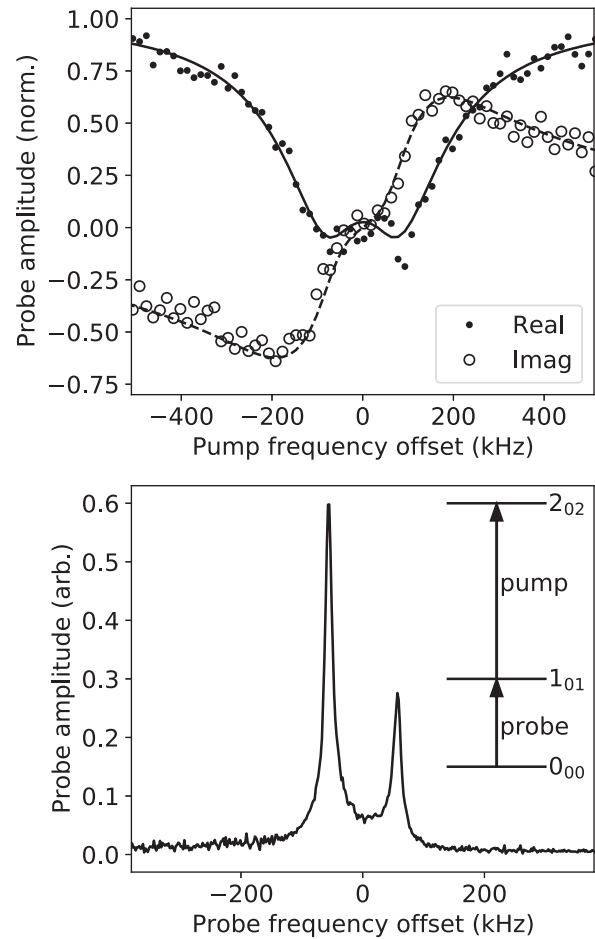


Figure 2. Laboratory measurements of the two lowest rotational transitions of $^{24}\text{MgC}_2$. The cavity-FTMW signal (bottom) centered at 20896.090 MHz is split into two Doppler components due to the coaxial cavity geometry. Its complex amplitude response (top) is plotted as a function of the double resonance pump frequency relative to 41711.852 MHz. The solid and dashed curves are the fitted saturated Lorentzian line profiles for the real and imaginary parts, respectively. Each panel represents 6.5 hr of integration or about 120,000 laser shots.

Table 1
Laboratory Rotational Frequencies of MgC_2

Isotopologue	Transition		Frequency (MHz)
	$J'_{KaKc} - J''_{KaKc}$	$F' - F''$	
$^{24}\text{Mg}^{12}\text{C}_2$	$1_{01} - 0_{00}$...	20896.090(2)
	$2_{02} - 1_{01}$...	41711.852(4)
$^{24}\text{Mg}^{13}\text{C}^{12}\text{C}$	$1_{01} - 0_{00}$...	20443.702(2)
$^{24}\text{Mg}^{13}\text{C}_2$	$1_{01} - 0_{00}$...	20027.207(2)
$^{25}\text{Mg}^{12}\text{C}_2$	$1_{01} - 0_{00}$	2.5 – 2.5	20509.780(4)
		3.5 – 2.5	20512.245(4)
		1.5 – 2.5	20513.305(4)
$^{26}\text{Mg}^{12}\text{C}_2$	$1_{01} - 0_{00}$...	20157.202(2)

Note. Estimated uncertainties are given in parentheses in units of the last digit.

structure, shown in Figure 1 (see Appendix A for details). The $1_{01} - 0_{00}$ transition of $^{25}\text{Mg}^{12}\text{C}_2$ is split into three hyperfine components by nuclear electric quadrupole interactions. The observed coupling constants are $\chi_{aa} = -11.75(2)$ MHz and $\chi_{bb} = 4.8(10)$ MHz, which agree well with the theoretical predictions of -11.4 MHz and 4.8 MHz, respectively.

Table 2
Lines of MgC₂ in IRC+10216

Isotopologue	Transition $J'_{K_a K_c} - J''_{K_a K_c}$	ν_{obs}^a (MHz)	$\nu_{\text{obs-calc}}$ (MHz)	E_u/k (K)	S	$\int T_A^* dv^b$ (mK km s ⁻¹)	θ_B ($''$)	η_B	W^c (mK km s ⁻¹)
²⁴ MgC ₂	2 ₀₂ - 1 ₀₁	41711.82 ± 0.02	-0.034	3.00	2.00	221 ± 10	42.5	0.53	1254 ± 138
	4 ₀₄ - 3 ₀₃	82787.94 ± 0.02	0.015	9.97	3.99	362 ± 10	29.7	0.853	841 ± 87
	4 ₂₃ - 3 ₂₂	83511.00 ± 0.15	-0.096	17.98	3.00	108 ± 11	29.5	0.853	249 ± 36
	4 ₂₂ - 3 ₂₁	84304.13 ± 0.04	0.105	18.04	3.00	149 ± 9	29.2	0.853	340 ± 40
	5 ₀₅ - 4 ₀₄	102907.74 ± 0.10	0.137	14.91	4.98	248 ± 8	23.9	0.853	476 ± 50
	5 ₄₂ - 4 ₄₁ ^d	104610.76 ± 0.30	-0.463	46.88	1.80	35 ± 8	23.5	0.853	65 ± 16
	5 ₄₁ - 4 ₄₀ ^d	104610.76 ± 0.30	-0.762	46.88	1.80	35 ± 8	23.5	0.853	65 ± 16
	5 ₂₃ - 4 ₂₂	105852.05 ± 0.15	-0.338	23.12	4.20	164 ± 9	23.2	0.853	308 ± 35
	6 ₀₆ - 5 ₀₅	122684.00 ± 0.50	-0.084	20.80	5.97	251 ± 30	20.1	0.785	463 ± 89
	7 ₀₇ - 6 ₀₆	142108.88 ± 0.10	-0.077	27.62	6.96	83 ± 6	17.3	0.785	141 ± 23
	7 ₂₅ - 6 ₂₄	149761.18 ± 0.20	-0.189	36.43	6.43	38 ± 7	16.4	0.785	63 ± 15
	²⁵ MgC ₂	2 ₀₂ - 1 ₀₁	40949.33 ± 0.20	-0.267	3.00	2.00	34 ± 5	42.5	0.53
4 ₀₄ - 3 ₀₃		79942.90 ± 0.30	0.171	9.62	3.99	41 ± 13	29.7	0.853	99 ± 33
²⁶ MgC ₂	2 ₀₂ - 1 ₀₁	40245.20 ± 0.20	-0.085	2.90	2.00	46 ± 8	42.5	0.53	261 ± 52
	5 ₀₅ - 4 ₀₄	99428.70 ± 0.40	-0.138	14.40	4.98	45 ± 10	29.7	0.853	89 ± 22

Notes. Unless otherwise noted, estimated uncertainties are 1σ . Frequencies subtracted from those observed are calculated from the constants in Table 3. E_u is the energy of the upper state of the transition, and S is the asymmetric rotor line strength; $\alpha_{J2000} = 09^{\text{h}}47^{\text{m}}57^{\text{s}}.36$, $\delta_{J2000} = +13^{\circ}16'44''.4$.

^a On the assumption of $v_{\text{LSR}} = -26.5$ km s⁻¹.

^b Derived from least-squares fits of shell profiles to the spectra shown in Figures 3 and 4; in some cases the expansion velocity was fixed to 14.5 km s⁻¹.

^c $W = \int T_A^* dv / \eta_B f_D$, where $f_D = \theta_S^2 / (\theta_S^2 + \theta_B^2)$ and the source diameter $\theta_S = 30''$. Errors include calibration uncertainties of 10% at 7 mm, 10% at 3 mm, and 15% at 2 mm, as well as an assumed error of 1 D on the dipole moment, added in quadrature.

^d Unresolved doublet with each component assumed to lie at the same frequency and possess half the intensity.

3. Astronomical Identification

With accurate laboratory data in hand, we examined available spectroscopic surveys and observations of IRC +10216 for evidence of MgC₂. An unidentified rotational line, U41712, coincident with the 2₀₂-1₀₁ transition of ²⁴MgC₂ was found in the recent 6–10 mm survey done by Pardo et al. (2022) using the Yebes 40 m telescope. A second unidentified line, U82788, was found in a study reporting the identification of the HC₄N radical (Cernicharo et al. 2004) using the IRAM 30 m telescope. Subsequently, eight additional unidentified lines were quickly found in unpublished surveys at 2 and 3 mm done with the IRAM 30 m telescope (see Cernicharo et al. 2019 for details) and assigned to ²⁴MgC₂. One line of ²⁵MgC₂ and three lines of ²⁶MgC₂ were also found at precisely the expected isotopic shifts.

There is overwhelming evidence that MgC₂ is the carrier of the lines listed in Table 2 and displayed in Figures 3 and 4. As Table 2 shows, a combined fit of the observed laboratory and astronomical lines of ²⁴MgC₂ to Watson’s A -reduced Hamiltonian yields small residuals corresponding to a normalized rms of 1.37 (Table 3), demonstrating that they originate from the same molecule. Table 3 lists the spectroscopic constants derived using only six free parameters (three rotational constants and three centrifugal distortion constants) and two parameters fixed to theoretical values. Similarly small residuals are obtained for ²⁵MgC₂ and ²⁶MgC₂, albeit with fewer determinable parameters given the small data sets. The ratio of the integrated intensities of the 2₀₂ - 1₀₁ lines of the three isotopologues is (73 ± 5):(11 ± 2):(15 ± 3), consistent with the solar abundance ratio of ²⁴Mg:²⁵Mg:²⁶Mg of (79.2 ± 0.6):(9.5 ± 0.5):(11.3 ± 0.5) (Bochsler et al. 1996) and the abundance ratio derived for MgNC in IRC+10216 itself, (78 ± 2):(11 ± 1):(11 ± 1) (Guélin et al. 1995).

Figures 3 and 4 present the astronomical spectra and show that the assigned lines meet all requirements of the

identification. Each line exhibits the same double-peaked or “U-shaped” profile and has the same width as the strong 4₀₄-3₀₃ line (29.0 ± 0.5 km s⁻¹) to within observational uncertainties. Six fully resolved or nearly fully resolved lines and four partially blended lines of ²⁴MgC₂ are detected. Three lines of ²⁶MgC₂ are detected, including one which is partially blended. Finally, one line of ²⁵MgC₂ is detected with a slightly broadened line width consistent with the underlying quadrupole hyperfine structure predicted from the laboratory measurements. The high quality profiles derived from the resolved lines and the precise rest frequencies of the blended lines allow us to account for the contributions of the interlopers and extract reliable parameters.

We have analyzed the intensities of the rotational lines to infer the excitation of the molecules on two assumptions: (1) to correct for the changing antenna beamwidth in Table 2, it is assumed by analogy with other Mg-bearing molecules in IRC +10216 that the MgC₂ emission is confined to a shell of 30'' in diameter (Cernicharo et al. 2019; Pardo et al. 2021), an assumption supported by the U-shaped profiles of the lines, and (2) all of the lines in Table 2 are optically thin because of their faintness.

4. Discussion

As Figure 1 shows, rotational emission lines spanning a wide range in energy are detected in IRC+10216, allowing us to construct the rotational temperature diagram shown in Figure 5. The integrated intensities of the lines are reproduced by a simple two-temperature excitation model (see Appendix B) in which a temperature $T_{\text{rot}} = 6 \pm 1$ K describes the relative populations within each K ladder and $T_{\text{kin}} = 22 \pm 13$ K describes the relative populations across K ladders and provides a measure of the gas kinetic temperature. A comparison of the derived excitation temperatures of MgC₂, SiC₂, and SiC₃ shows that T_{rot} is similar for the three species (6 ± 1 K versus

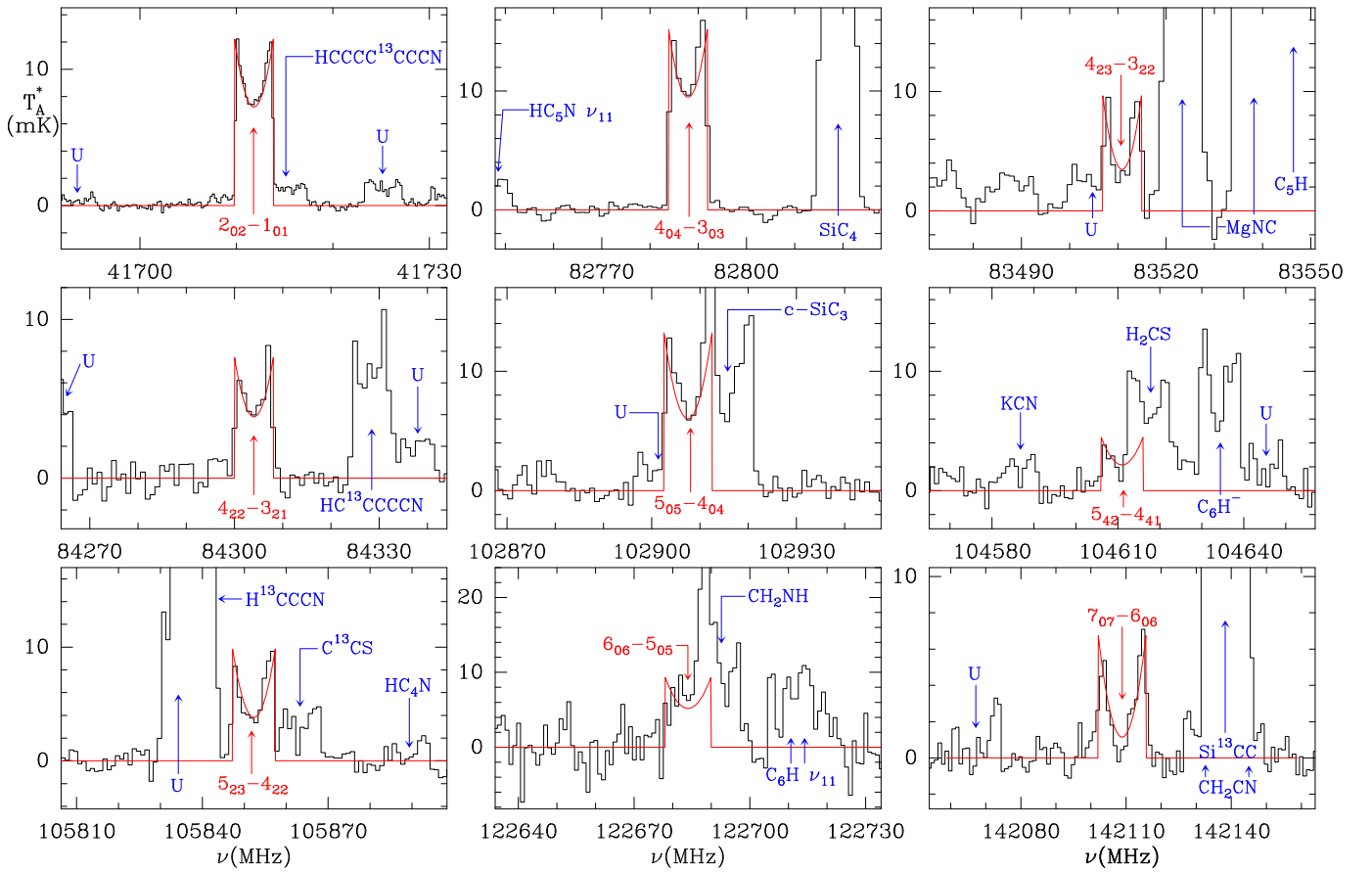


Figure 3. Spectra of $^{24}\text{MgC}_2$ toward IRC+10216. The fitted profiles are plotted in red. “U” indicates unidentified lines.

10 K and 13 K; Thaddeus et al. 1984; Apponi et al. 1999), but T_{kin} is not. The latter is similar for MgC_2 and SiC_3 (22 ± 13 K and 46 K; Apponi et al. 1999), and it is significantly smaller than for SiC_2 (140 K; Thaddeus et al. 1984), probably because MgC_2 and SiC_3 reside in the cool outer envelope of IRC+10216, whereas SiC_2 is more widely distributed, residing in the warmer inner regions as well as the outer envelope (Patel et al. 2011). The T_{kin} of 22 K inferred for MgC_2 is remarkably close to the value of 20 K inferred from observations and modeling of dust, CO, and CCH in the $30''$ – $40''$ diameter shell of IRC+10216 (Guélin et al. 2018). As discussed in Appendix B, the column density averaged over a $30''$ antenna beam is $N(\text{MgC}_2) = 1 \times 10^{12} \text{ cm}^{-2}$, with an estimated uncertainty of 30%, corresponding to a fractional abundance of $\sim 5 \times 10^{-10}$ relative to H_2 .⁶

On the assumption that MgC_2 is cospatial with the magnesium–carbon chain radicals MgCCH , MgC_4H , and MgC_6H (which is supported by the similar line profiles), a comparison of their abundances might shed light on the production of Mg-bearing species in the outer envelope of IRC+10216. The formation of MgCCH , MgC_4H , and MgC_6H has been explained by a two-step process in which radiative association (RA) of Mg^+ with large polyynes HC_{2n}H ($n \geq 4$) yields the intermediate ions $\text{MgHC}_{2n}\text{H}^+$, which then undergo dissociative recombination (DR) to yield the neutral radicals (Cernicharo et al. 2019; Pardo et al. 2021). This mechanism, originally proposed by Petrie (1996) and later expanded by Dunbar & Petrie (2002), is thought to control the formation of

the metal cyanides and acetylides detected in IRC+10216 (Millar 2008; Cabezas et al. 2013; Cernicharo et al. 2019; Pardo et al. 2021). The chemical models developed in these studies indicate that the main precursors of magnesium–carbon chains are large $\text{MgHC}_{2n}\text{H}^+$ complexes with more than six carbon atoms. If, as is plausible, MgC_2 is also a fragmentation product in the DR of $\text{MgHC}_{2n}\text{H}^+$, then the observed column density ratio $\text{MgC}_2:\text{MgCCH}:\text{MgC}_4\text{H}:\text{MgC}_6\text{H} = 1:2:22:20$ provides a useful constraint on the relative yields of the DR of the parent ions. Observations of other plausible DR products, such as MgC and larger MgC_n clusters are needed to better elucidate the poorly constrained gas-phase chemistry. A parallel formation mechanism that may also be important is the RA–DR of Mg^+ and large cyanopolynes, HC_{2n+1}N (Dunbar & Petrie 2002). Experimental measurements of the branching ratios of the various fragments formed in the DR of large $\text{MgHC}_{2n}\text{H}^+$ and $\text{MgHC}_{2n+1}\text{NH}^+$ ions would enable a direct comparison against the observed abundance ratios, permitting a holistic assessment of the production of metal-bearing molecules in the outer layers of IRC+10216.

Understanding the structure and bonding in metal dicarbides is of fundamental chemical interest and may identify additional metal carbides that are candidates for astronomical detection. Like other T-shaped triatomic dicarbides, including SiC_2 (Cernicharo et al. 1991), GeC_2 (Zingsheim et al. 2017), BeC_2 (Green et al. 2020), AlC_2 (Halfen & Ziurys 2018), ScC_2 (Min et al. 2014), and YC_2 (Halfen et al. 2013), MgC_2 exhibits an ionic metal–carbon bond best described as Mg^+-C_2^- . Its equilibrium CC bond length, $r_{\text{CC}} = 1.2706(7) \text{ \AA}$, is close to that of bare C_2^- itself, $r_{\text{CC}} = 1.26831(13) \text{ \AA}$ (Rehfuß et al. 1988),

⁶ We adopt $N(\text{H}_2) = 2.1 \times 10^{21} \text{ cm}^{-2}$ following Gong et al. (2015).

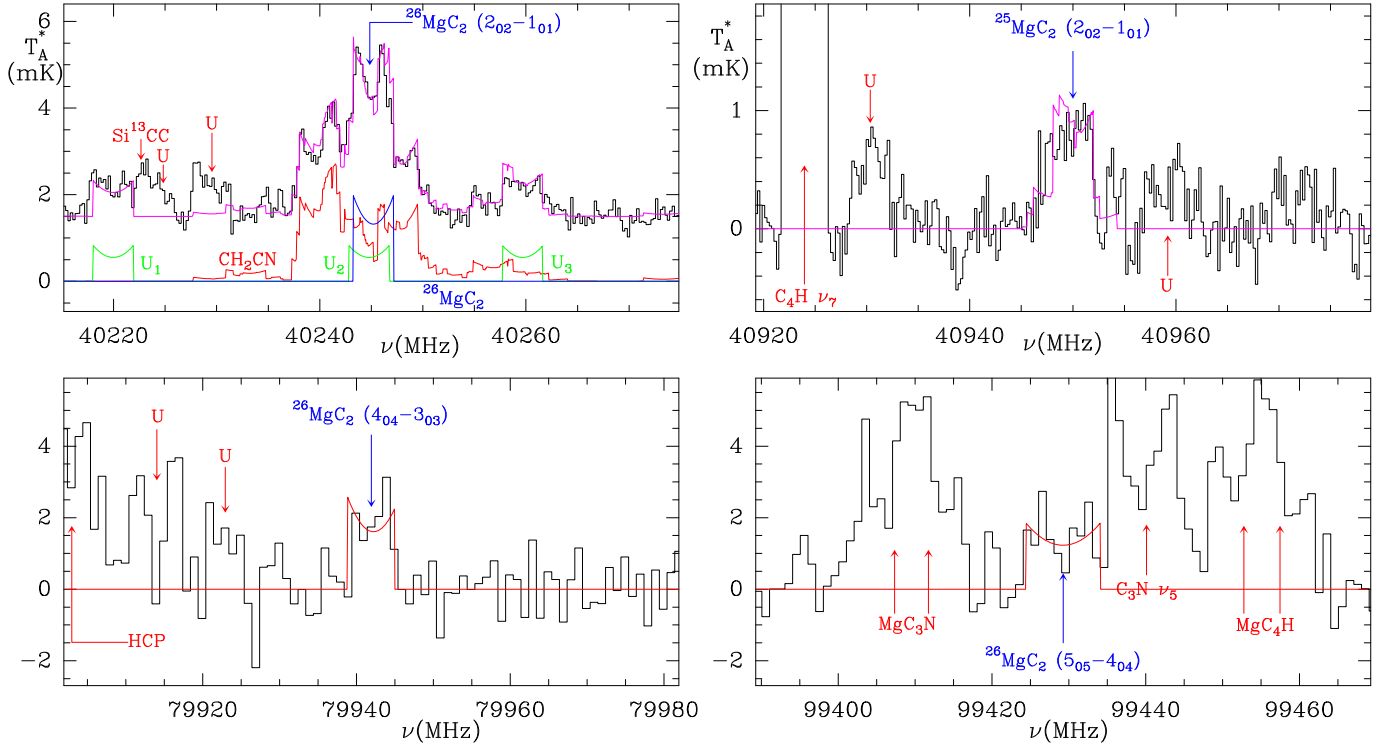


Figure 4. Spectra of $^{25}\text{MgC}_2$ and $^{26}\text{MgC}_2$ toward IRC+10216. The simulated profile of the $2_{02} - 1_{01}$ transition of $^{26}\text{MgC}_2$ (shown in blue in the top left panel) accounts for contamination from overlapping CH_2CN transitions (shown in red); the total emission is shown in magenta. The profile for $^{25}\text{MgC}_2$ (top right) includes quadrupole hyperfine splittings calculated from the laboratory constants. “U” indicates unidentified lines.

which are both significantly longer than neutral C_2 , $r_{\text{CC}} = 1.24244(1)$ Å (Douay et al. 1988). Moreover, the ionicity, defined as the ratio of the molecular dipole moment to the dipole moment resulting from unit point charges separated by the metal- C_2 bond length, $i = \mu / e r_{\text{Mg}-\text{C}_2} = 0.86$, suggests the nearly complete transfer of a $3s$ electron from Mg to the C_2 fragment.

The bonding in MgC_2 closely resembles that in MgO (Boldyrev & Simons 1997), with the in-plane π_u orbital of C_2 taking the place of the $2p_z$ orbital of O. MgO has a similar ionicity, $i = 0.72$, and Mg nuclear quadrupole coupling constant: $-10(4)$ MHz (Törring & Hoeft 1986) versus $\chi_{\text{aa}} = -11.72(2)$ MHz for MgC_2 . These latter parameters indicate that the Mg $3s$ orbital in both molecules is substantially hybridized. Given that the atomic $3p_z$ orbital of Mg^+ has a quadrupole coupling constant of -46 MHz (Sur et al. 2005), the p character is about 25%. Although simple orbital descriptions of MgC_2 and MgO are potentially obscured by their multiconfigurational, mixed ionic-covalent character (Thümmel et al. 1989; Itono et al. 2000), this issue appears to be less severe for MgC_2 , which is adequately described with single-reference coupled cluster methods as borne out by the calculations in this work and others (Woon 1996). The bonding of the heavier group IIA dicarbides CaC_2 and SrC_2 can be expected to follow the same trends observed in their respective oxides. Because of their high ionicities, all of these species possess unusually large dipole moments (Fuentelba & Savin 2000).

Observations of MgC_2 and similar metal dicarbides are a promising means to elucidate the role of metals in the chemistry of IRC+10216, as well as the state of refractory elements in carbon-rich circumstellar environments more generally. Metals are inferred to be significantly depleted onto

Table 3
Spectroscopic Constants of MgC_2

Constant	$^{24}\text{MgC}_2$	$^{25}\text{MgC}_2$	$^{26}\text{MgC}_2$
Rotational and centrifugal distortion constants (MHz):			
A	51900(1)	51899.8 ^b	51897.6 ^b
$(B + C)/2$	10448.0740(9)	10255.8294(12)	10078.601(1)
$(B - C)/4$	526.033(14)	507.046 ^b	490.890(61)
$10^3 \Delta_J$	14.454(101)
$10^3 \Delta_{JK}$	245.12(169)
$10^3 \Delta_K$	-37.84^a
$10^3 \delta_J$	0.369(168)
$10^3 \delta_K$	148.03 ^a
Electric quadrupole coupling constants (MHz):			
χ_{aa}	...	$-11.75(2)$...
χ_{bb}	...	4.8(10)	...
σ_{nrms}	1.37	0.29	0.40
Inertial defect ($\text{amu}\cdot\text{Å}^2$):			
Δ	0.1035(3)	0.1037	0.125(1)

Notes. Constants are derived from a least-squares fit to the rotational transitions in Tables 1 and 2. The 1σ uncertainties are indicated in parentheses, with the least significant digit corresponding to the least significant digit of the value. Parameters for which no errors are indicated have been fixed to the theoretical values.

^a Second-order vibrational perturbation theory (VPT2) value at the CCSD(T)/cc-pVTZ level of theory.

^b Fixed to the experimental values derived from $^{24}\text{MgC}_2$; the equilibrium isotope shift was taken from the semiexperimental equilibrium structure, and the zero-point correction from the variational calculations (Appendix A).

dust grains in IRC+10216 (Mauron & Huggins 2010), yet even the residual gas-phase abundance of metal atoms and ions is sufficient to drive a rich chemistry. For example, molecules

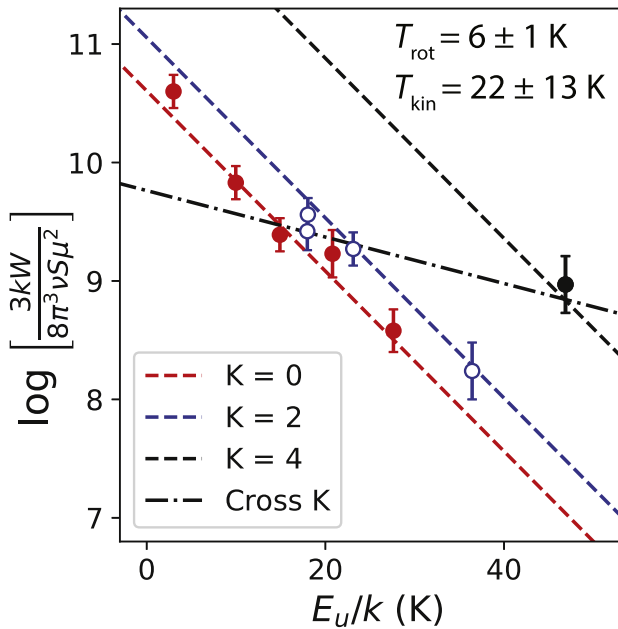


Figure 5. Rotational temperature diagram of $^{24}\text{MgC}_2$ in IRC+10216, fitted with the two-temperature model described in Appendix B. The slope of the parallel lines through each K ladder yields the rotational temperature (T_{rot}), and the slope of the line through points across the K ladders yields the kinetic temperature (T_{kin}). The flux of the $K = 4$ transition is assumed to be one-half the total flux of the unresolved $5_{42} - 4_{41}/5_{41} - 4_{40}$ doublet. The error bar on each data point is twice the error shown in Table 2. Error bars on the parameters are twice the standard error of the fit.

containing the cyano radical (CN) bonded to the most abundant metallic elements (Na, K, Mg, Ca, Al, and Fe) have been found there. Given that the abundances of MgC_2 and MgNC (Guélin et al. 1995) are within an order of magnitude of each other, it is very likely that other metal dicarbides are also synthesized in the external layers of the circumstellar envelope of IRC+10216, plausibly following the same chemical pathway that is postulated to yield MgC_2 . By analogy with SiC_2 , which has yielded invaluable information on gas-phase processes within the inner and intermediate winds, as well as the outer circumstellar envelopes of evolved carbon-rich stars (Massalkhi et al. 2018, and references therein), metal dicarbides may also serve as important probes provided their excitation, abundance, and distribution are understood. The distribution of metal dicarbides as a function of radial distance from the central star in IRC+10216, for example, accompanied by a careful analysis of their abundance and excitation might shed light on processes such as condensation and dust formation, which remain poorly understood.

The identification of MgC_2 in the laboratory and in space marks a key step in the study of metal carbides and suggests that other highly polar metal-carbon molecules might be detectable. After MgC_2 , CaC_2 is the next most promising candidate for detection because it possesses an even larger dipole moment (10.7 D; Fuentealba & Savin 2000) than MgC_2 (7.9 D; Itono et al. 2000) and because Ca is cosmically the next most abundant group IIA element after Mg; calcium isocyanide (CaNC) has already been detected in IRC+10216 (Cernicharo et al. 2019), suggesting that other Ca-bearing molecules may be present there. By analogy with SiC (Massalkhi et al. 2018), the monocarbides MgC and CaC may be important for comparative studies of the distribution, abundance, and photochemical processing of dicarbides in circumstellar envelopes; although

CaC has been detected in the laboratory, MgC has not, and its astronomical detection might be more feasible given the higher abundance of Mg. Other promising systems for study include larger metal-carbon clusters such as MgC_n about which little is known experimentally, but which, like the silicon-carbon clusters SiC_3 and SiC_4 (Apponi et al. 1999; Gordon et al. 2000), are amenable to laboratory characterization and astronomical detection.

We are indebted to Dr. Marie-Aline Martin-Drumel (CNRS) for her valuable assistance with the initial laboratory efforts and comments on the manuscript, and to Dr. Carl Gottlieb (CfA) for helpful discussions. P.B.C. and M.C.M. are supported by the National Science Foundation (award Nos. AST-1908576 and PHY-2110489). H.G. acknowledges support from the National Science Foundation for participation in this work as part of his independent research and development plan. Any opinions, findings, and conclusions expressed in this material are those of the authors and do not necessarily reflect the views of the National Science Foundation. We acknowledge funding support from the Spanish Ministerio de Ciencia e Innovación through grants PID2019-107115GB-C21 and PID2019-106110GB-I00.

Appendix A

Structure Calculations and Semiexperimental Equilibrium Geometry

Coupled cluster calculations were performed using the CFOUR package (Matthews et al. 2020) at the singles, doubles, and perturbative triples (CCSD(T)) level of theory (Raghavachari et al. 1989) with the cc-pCVXZ ($X = \text{D, T, Q, 5}$) basis sets (Woon & Dunning 1995; Prascher et al. 2011) correlating all but the Mg 1s electrons. The complete basis set equilibrium geometry was estimated by an exponential extrapolation of the entire $X = \text{D-5}$ sequence. To derive a semiexperimental equilibrium geometry, vibrational corrections to the rotational frequencies were determined by variational rovibrational calculations on a potential energy surface (PES) fitted to 448 CCSD(T)/cc-pCVQZ single-point energies using the NITROGEN package (Changala 2021). Additional contributions to the rotational constants from the rotational g -tensor (Gauss & Puzzarini 2010) were computed with the cc-pCVTZ basis set, and nuclear electric quadrupole coupling constants with the cc-pCV5Z basis set.

The small number of laboratory transitions observed for each isotopologue is insufficient to determine a complete set of experimental rotational constants. Instead, the structure determination was performed by least-squares fitting directly to the transition frequencies. That is, a proposed equilibrium geometry was used to compute equilibrium rotational constants, which were then corrected by the rotational g -tensor. These in turn were used to generate rigid-rotor transition frequencies, to which the vibrational corrections from the rovibrational variational calculations were added. These latter corrections are defined as the difference between the variational transition energies and the rigid-rotor transition energies based on the equilibrium geometry of the same PES. They therefore include both vibrational zero-point and centrifugal distortion effects. For $^{25}\text{MgC}_2$, the degeneracy-weighted mean of the quadrupole-split energies was used as the hyperfine-free value. The optimized structural parameters are shown in Figure 1 and compared to the extrapolated CCSD(T) geometry in Table 4. These parameters reproduce the six laboratory frequencies with

Table 4
The Equilibrium Geometry of MgC₂

Basis Set	r_{CC}	r_{Mg-C_2}
D	1.29422	1.96504
T	1.27545	1.92117
Q	1.27175	1.91073
5	1.27082	1.90741
CBS	1.27068	1.90673
r_{se}	1.2706(7)	1.9066(1)

Note. The CCSD(T)/cc-pCVXZ bond lengths (in Å) are shown for $X = D-5$, followed by the complete basis set (CBS) extrapolation. The semiexperimental equilibrium geometry (r_{se}) was determined as discussed in the text; r_{CC} is the C-C distance and r_{Mg-C_2} is the distance between Mg and the CC center of mass.

an rms residual of 0.1 MHz. This is significantly larger than the experimental uncertainty (2 kHz) indicating that the theoretical corrections are the dominant source of error.

Appendix B

Two-temperature Model for Rotational Excitation

In the analysis of rotational emission of prolate asymmetric tops such as MgC₂ the partitioning of energy levels within and across radiatively decoupled rotational manifolds must be taken into account. Because radiative transitions are confined within the K ladders but collisional transitions occur within and across the ladders, the rotational excitation temperature within the ladders (T_{rot}) is not necessarily equal to the excitation temperature across the ladders, which is assumed equal to the kinetic temperature (T_{kin}) of the gas. For highly polar species, excitation within the ladders is highly subthermal (i.e., $T_{rot} \ll T_{kin}$) because collisional excitation is much slower than spontaneous radiative decay. Let T_{kin} describe the population distribution across K ladders and T_{rot} describe the population distribution within each K ladder. Then, the intensity of an optically thin rotational line is given by



$$\frac{3kW}{8\pi^3\nu S\mu^2} = \frac{Ne^{-E_l/kT_{rot}}e^{-E_K/kT_{kin}}}{Z}, \quad (B1)$$

where $W = \int T_{MB} dv$ is the main beam temperature integrated over the radial velocity, ν is the line frequency, S is the rotational line strength, μ is the dipole moment, and N is the total column density. The Boltzmann factors and partition function, Z , in Equation (B1) are calculated by splitting the total rotational energy into two parts, $E_u = E_K + E_J$, where $E_K = (A - (B + C)/2)K^2$ is the K -dependent part, and E_J is the remainder. Taking the logarithm of Equation (B1) yields

$$\log \frac{3kW}{8\pi^3\nu S\mu^2} = \log \frac{N}{Z} - \frac{(E_u - E_K) \log e}{kT_{rot}} - \frac{E_K \log e}{kT_{kin}}. \quad (B2)$$

A least-squares fit of Equation (B2) to the integrated intensities (W) from Table 2 yields $T_{rot} = 5.71 \pm 1.12$ K and $T_{kin} = 22.14 \pm 13.08$ K, which are shown rounded off in the rotational temperature diagram of Figure 5. Multiplying the intercept $\log(N/Z) = 10.60$ by the partition function $Z(T_{rot}, T_{kin}) = 24.59$ evaluated numerically as a sum over states yields $N(\text{MgC}_2) = 1 \times 10^{12} \text{ cm}^{-2}$. We estimate the total uncertainty in N from the dipole moment (7.9 ± 1.0 D) and excitation conditions to be 30%.

ORCID iDs

P. B. Changala  <https://orcid.org/0000-0003-0304-9814>
H. Gupta  <https://orcid.org/0000-0003-2588-516X>
J. Cernicharo  <https://orcid.org/0000-0002-3518-2524>
J. R. Pardo  <https://orcid.org/0000-0003-4639-8440>
M. Agúndez  <https://orcid.org/0000-0003-3248-3564>
C. Cabezas  <https://orcid.org/0000-0002-1254-7738>
B. Tercero  <https://orcid.org/0000-0002-4782-5259>
M. Guélin  <https://orcid.org/0000-0002-4896-500X>

References

- Apponi, A. J., McCarthy, M. C., Gottlieb, C., & Thaddeus, P. 1999, *ApJ*, **516**, L103
- Bochsler, P., Gonin, M., Sheldon, R. B., et al. 1996, in AIP Conf. Proc. 382, Solar Wind Eight (Melville, NY: AIP), 199
- Boldyrev, A. I., & Simons, J. 1997, *JPCA*, **101**, 2215
- Brünken, S., Müller, H. S. P., Menten, K. M., McCarthy, M. C., & Thaddeus, P. 2008, *ApJ*, **676**, 1367
- Cabezas, C., Cernicharo, J., Alonso, J. L., et al. 2013, *ApJ*, **775**, 133
- Cernicharo, J., Cabezas, C., Pardo, J., et al. 2019, *A&A*, **630**, L2
- Cernicharo, J., Guélin, M., Kahane, C., et al. 1991, *A&A*, **246**, 213
- Cernicharo, J., Guélin, M., & Pardo, J. R. 2004, *ApJ*, **615**, L145
- Changala, P. B. 2021, bchangala/nitrogen: NITROGEN v2.1.2, Zenodo, doi:10.5281/zenodo.7342277
- Crabtree, K. N., Martin-Drumel, M., Brown, G. G., et al. 2016, *JChPh*, **144**, 124201
- Douay, M., Nietmann, R., & Bernath, P. F. 1988, *JMoSp*, **131**, 250
- Dunbar, R. C., & Petrie, S. 2002, *ApJ*, **564**, 792
- Fuentealba, P., & Savin, A. 2000, *JPCA*, **104**, 10882
- Gauss, J., & Puzzarini, C. 2010, *MolPh*, **108**, 269
- Gong, Y., Henkel, C., & Spezzano, S. e. a. 2015, *A&A*, **574**, A56
- Gordon, V. D., Nathan, E. S., Apponi, A. J., et al. 2000, *JChPh*, **113**, 5311
- Grabow, J. U., Palmer, E. S., McCarthy, M. C., & Thaddeus, P. 2005, *RSci*, **76**, 093106
- Green, M. L., Jaffe, N. B., & Heaven, M. C. 2020, *J. Phys. Chem. Lett.*, **11**, 88
- Green, S. 1984, *CPL*, **112**, 29
- Guélin, M., Forestini, M., Valiron, P., et al. 1995, *A&A*, **297**, 183
- Guélin, M., Patel, N. A., Bremer, M., et al. 2018, *A&A*, **610**, A4
- Halfen, D. T., Min, J., & Ziurys, L. M. 2013, *CPL*, **555**, 31
- Halfen, D. T., & Ziurys, L. M. 2018, *PCCP*, **20**, 11047
- Itono, S., Takano, K., Hirano, T., & Nagashima, U. 2000, *ApJL*, **538**, L163
- Kawaguchi, K., Kagi, E., Hirano, T., Takano, S., & Saito, S. 1993, *ApJ*, **406**, L39
- Kleman, B. 1956, *ApJ*, **123**, 162
- Lee, K. L. K., Thorwirth, S., Martin-Drumel, M. A., & McCarthy, M. C. 2019, *PCCP*, **21**, 18911
- Massalkhi, S., Agúndez, M., & Cernicharo, J. e. a. 2018, *A&A*, **611**, A29
- Mathews, D. A., Cheng, L., Harding, M. E., et al. 2020, *JChPh*, **152**, 214108
- Mauron, N., & Huggins, P. J. 2010, *A&A*, **513**, A31
- Millar, T. J. 2008, *Ap&SS*, **313**, 223
- Min, J., Halfen, D. T., & Ziurys, L. M. 2014, *CPL*, **609**, 70
- Pardo, J. R., Cabezas, C., Fonfría, J. P., et al. 2021, *A&A*, **652**, L13
- Pardo, J. R., Cernicharo, J., Tercero, B., et al. 2022, *A&A*, **658**, A39
- Patel, N. A., Young, K. H., Gottlieb, C. A., et al. 2011, *ApJS*, **193**, 17
- Petrie, S. 1996, *MNRAS*, **282**, 807
- Prascher, B. P., Woon, D. E., Peterson, K. A., Dunning, T. H., & Wilson, A. K. 2011, *Theor. Chem. Acc.*, **128**, 69
- Raghavachari, K., Trucks, G. W., Pople, J. A., & Head-Gordon, M. 1989, *CPL*, **157**, 479
- Rehfuß, B. D., Liu, D. J., Dinelli, B. M., et al. 1988, *JChPh*, **89**, 129
- Sun, M., Halfen, D. T., Min, J., et al. 2010, *JChPh*, **133**, 174301
- Sur, C., Sahoo, B. K., Chaudhuri, R. K., Das, B. P., & Mukherjee, D. 2005, *EPJD*, **32**, 25
- Thaddeus, P., Cummins, S. E., & Linke, R. A. 1984, *ApJ*, **23**, L45
- Thümmel, H., Klotz, R., & Peyerimhoff, S. D. 1989, *CP*, **129**, 417
- Törring, T., & Hoefl, J. 1986, *CPL*, **126**, 477
- Woon, D. E. 1996, *ApJ*, **456**, 602
- Woon, D. E., & Dunning, T. H. 1995, *J. Chem. Phys.*, **103**, 4572
- Zingsheim, O., Martin-Drumel, M. A., Thorwirth, S., et al. 2017, *J. Phys. Chem. Lett.*, **8**, 3776
- Ziurys, L. M., Apponi, A. J., Guélin, M., & Cernicharo, J. 1995, *ApJ*, **445**, L47